International Journal of Minerals, Metallurgy and Materials
Volume 26, Number 11, November 2019, Page 1477
https://doi.org/10.1007/s12613-019-1889-3

Tungsten nanoparticle-strengthened copper composite prepared by a sol–gel method and *in-situ* reaction

Tian-xing Lu[1)], *Cun-guang Chen*[1)], *Zhi-meng Guo*[1)], *Pei Li*[1)], *and Ming-xing Guo*[2)]

1) Institute for Advanced Materials and Technology, University of Science and Technology Beijing, Beijing 100083, China
2) State Key Laboratory for Advanced Metals and Materials, University of Science and Technology Beijing, Beijing 100083, China
(Received: 28 June 2019; revised: 22 August 2019; accepted: 30 August 2019)

Abstract: Tungsten nanoparticle-strengthened Cu composites were prepared from nanopowder synthesized by a sol–gel method and *in-situ* hydrogen reduction. The tungsten particles in the Cu matrix were well-dispersed with an average size of approximately 100–200 nm. The addition of nanosized W particles remarkably improves the mechanical properties, while the electrical conductivity did not substantially decrease. The Cu–W composite with 6wt% W has the most comprehensive properties with an ultimate strength of 310 MPa, yield strength of 238 MPa, hardness of HV 108 and electrical conductivity of 90% IACS. The enhanced mechanical property and only a small loss of electrical conductivity demonstrate the potential of this new strategy to prepare W nanoparticle-strengthened Cu composites.

Keywords: copper composites; second phase strengthening; tungsten; sol–gel method

1. Introduction

Copper composites have been widely utilized as electrodes, heat sink materials, or electrical contact materials because of their excellent electrical conductivity. However, the applications of copper composites are limited owing to their inadequate mechanical properties and thermal stability [1–3]. To overcome these shortcomings, strengthening mechanisms, such as solid solution strengthening, cold work strengthening, and second phase strengthening, have been used to reinforce the copper alloys [4–5]. Compared to copper alloys prepared by other strengthening mechanisms, second phase strengthened copper alloys have advantages of high strength, excellent thermal stability, and enhanced electrical conductivity [6–8]. Researchers have recently investigated many candidates of dispersed particles including metal oxides such as Al_2O_3, Y_2O_3, and ZrO_2 [9–14], metal nitrates such as TiN [15] and metal carbides such as SiC [16].

The second phase should have high thermodynamic stability, insolubility in a copper matrix and positive effect for enhancing creep resistance [17]. Tungsten has advantages of an ultrahigh melting temperature (about 3700 K), optimal electrical conductivity (greater than 30% IACS), ideal creep resistance, and immiscibility with a copper matrix [18–19]. Therefore, tungsten can be a prime candidate as a second phase dispersion particle due to its excellent overall properties. Recently, W particle strengthened copper alloys prepared by ball milling have been reported, but the homogeneity of the second phase is not optimized [20–21]. Among existing synthesis processes, the sol–gel method has remarkable merits, such as high purity, homogeneous distribution, and an ultrafine powder size. Guo *et al.* [22] successfully synthesized a nano-scale W–Cu powder with average size smaller than 150 nm using the sol–gel method. Jiang *et al.* [23] also proved the feasibility of using the sol–gel method for the synthesis of nanosized metals. As a result, the sol–gel method is expected to become a promising process for the preparation of W nanoparticle-strengthened copper.

In this study, W nanoparticle-strengthened Cu composites were prepared by a sol–gel method, hydrogen reduction of Cu–W oxide, and spark plasma sintering (SPS). The microstructure, tensile strength, microhardness, and electrical

Corresponding authors: Zhi-meng Guo E-mail: zmguo@ustb.edu.cn; Cun-guang Chen E-mail: cgchen@ustb.edu.cn

conductivity were measured. The results show that the W nanoparticle-strengthened Cu composites were successfully synthesized and the well-dispersed W nanoparticles effectively reinforced the Cu matrix without significant loss of the electrical conductivity.

2. Experimental

Raw materials comprised of copper nitrate $Cu(NO_3)_2{\cdot}3H_2O$, ammonium tungstate $(NH_4)_{10}W_{12}O_{41}{\cdot}xH_2O$ (AMT), and citric acid as a chelating agent were used for the preparation of Cu composites with 3wt% W (Cu–3W), 6wt% W (Cu–6W), and 10wt%W (Cu–10W). $Cu(NO_3)_2{\cdot}3H_2O$, AMT, and citric acid were added to distilled water and heated at 120°C to form a wet sol. The mixed sol was then heated and dried at 150°C for 24 h to acquire the dry gel. The dry gel was heated further at 300°C for 2 h in air to synthesize the mixed oxide powders. After ball milling for 2 h, the mixed oxide powders were reduced under an H_2 atmosphere for 1 h at 800°C to generate the W nanoparticle-strengthened Cu powders. The powders were sintered by SPS at 800°C for 5 min at 40 MPa. For comparison, a pure copper sample was also prepared using the same method.

To elucidate the phase transformation procedure, thermogravimetric and differential scanning calorimetry (TG-DSC) analysis were conducted in an air atmosphere from room temperature to 400°C at the heating speed of 10°C/min (TA Discovery 25). The microstructure of the powders and bulk composites were characterized by field emission scanning electron microscopy (FE-SEM, Zeiss Supra^{TM}55) with back-scattered electron imaging (BSE) mode and energy dispersive spectrometry (EDS), along with transmission electron microscopy (TEM, FEI Tecnai G2-F20) at 200 keV under a high-angle annular dark field (HAADF) mode. The average grain size of the bulk composites was also determined by SEM. X-ray diffraction (XRD, Rigaku TTR III) was used to investigate the powder phase of the dry gel, mixed oxide powder, and copper composite powder reduced at different temperatures using Cu Kα radiation. The electrical conductivity of the specimens was measured by a four-probe method (TH2513A). The tensile strength and Vickers hardness (with a load of 4.9 N) were also measured from the average of at least three samples of each Cu–W composite.

3. Results and discussion

3.1. Thermodynamic analysis of the Cu–W system

To illustrate the formation of the two separate phases of the Cu matrix and dispersed W particles, the formation enthalpy (ΔH), entropy (ΔS), and Gibbs free energy (ΔG) were calculated by a Miedema mode of the Cu–W composites with different compositions [24–25]. Fig. 1 shows the ΔH, ΔS, and ΔG with the change in W content at 273 K. The Gibbs free energy was calculated by:

$$\Delta G = \Delta H - T\Delta S \quad (1)$$

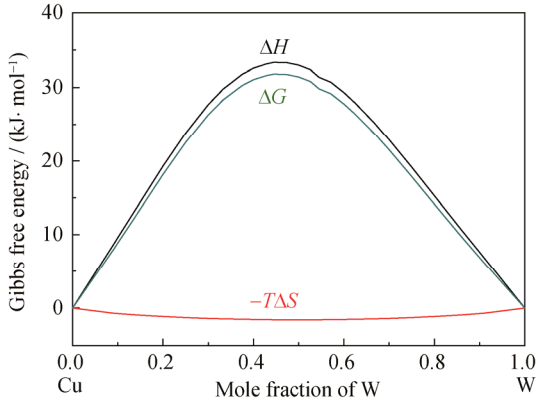

Fig. 1. Gibbs free energy change of the Cu–W binary system calculated by the Miedema mode.

In the Cu–W binary system, the total formation enthalpy and Gibbs free energy was positive at all compositions. The Gibbs free energy of the Cu–W system reached up to 31.4 kJ/mol at 273 K. Even at the melting temperature of copper (1356 K), the Gibbs free energy of Cu–W system was still up to 25.2 kJ/mol, which meant that it is not possible to form the equilibrium Cu–W solid solution. Therefore, the Miedema mode calculation proved that the W particles would be stable in the copper matrix.

In this preparation method, the transformation of the dry gel to mixed oxide was characterized by TG-DSC. Fig. 2 shows the TG-DSC curve of the Cu–10W dry gel from room temperature to 400°C. The weight loss of the dry gel started from 60°C due to the water evaporation. The main weight loss and exothermic peak occurred at 210°C, which indicates that the oxidation reaction of the dry gel was complete at 210°C. After the oxidation reaction, the oxide powder was generated with a mixture of CuO and $CuWO_4$.

Following previous studies, the reduction of copper tungstate occurred according to the following reaction [26–27]:

$$CuWO_4 + H_{2(g)} \rightarrow Cu + WO_3 + H_2O;$$
$$\Delta G = 59015 + 340.1T - 83.9T\ln T + 20.9\times10^{-3}T^2 - 8.2\times10^5 T^{-1} \quad (2)$$
$$WO_3 + H_{2(g)} \rightarrow W + H_2O_{(g)};$$
$$\Delta G = 117469 - 446.9T + 49.9T\ln T - 10.7\times10^{-3}T^2 + 8.5\times10^5 T^{-1} \quad (3)$$

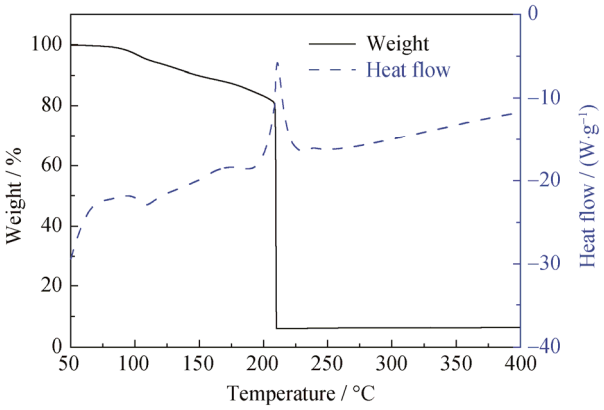

Fig. 2. TG-DSC curve of Cu–10W dry gel from room temperature to 400°C.

Fig. 3 shows the Gibbs free energy of these two reactions. According to the calculation, the ΔG of reaction (2) will be always negative as long as the temperature above 0°C, but the ΔG of reaction (3) will be negative only when the temperature greater than 800°C. In the reduction process, different tungsten oxide components were produced at different temperatures.

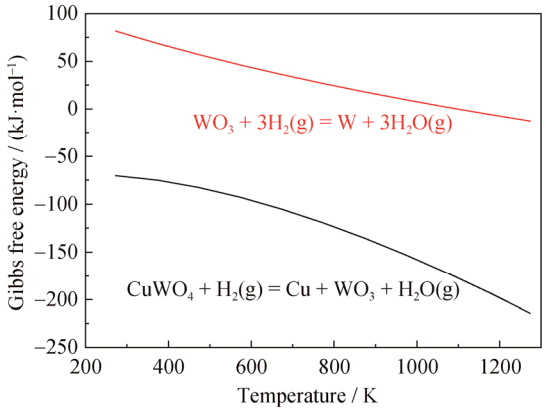

Fig. 3. Gibbs free energy of reaction (2) and reaction (3).

3.2. Powder and bulk composite microstructures

The XRD patterns of the dry gel, mixture oxide powder, and composite powder reduced at 350°C, 700°C, and 800°C in an H_2 atmosphere for 1 h are shown in Fig. 4 for the Cu–10W composite. As illustrated by the patterns, the mixture of copper tungstate and copper oxide were generated in the dry gel. Fig. 4 shows that the mixture of $CuWO_4$ and CuO were reduced to generate Cu and WO_3 at 350°C; Cu and WO_2 at 700°C. At 800°C, the mixed oxides were fully reduced into the Cu–W composite powder.

The microstructures of the Cu–10W mixed oxide powders and reduced Cu–10W powder are shown in Fig. 5(a) and Fig. 5(b), respectively. As shown in Fig. 5(a), the mixed oxide powder was an agglomeration of nanosized oxide powder smaller than 200 nm. Fig. 5(b) shows the microstructure of hydrogen reduced Cu–10W powder. After hydrogen reduction, the W nanoparticles were dispersed on the surface of ultrafine Cu powders and the size of the W particle was approximately 100 nm. The size of the W particles significantly decreased from the oxide powder to reduced composite powder, which might be due to the gas phase transfer reaction of W oxides [28–29]. In this reaction, reduced W oxides will evaporate and then nucleate on the surface of Cu powders via a chemical vapor transports mechanism. Based on this mechanism, the size of the reduced W particle depends on the content and uniformity of WO_3.

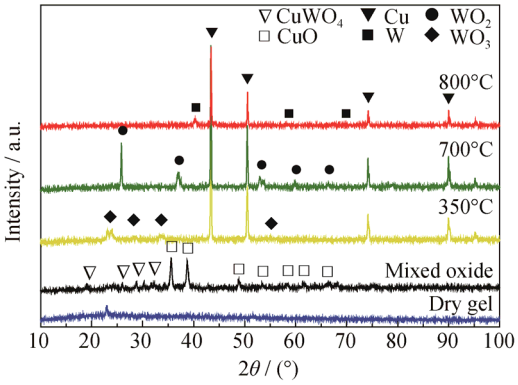

Fig. 4. XRD patterns of the Cu–10W dry gel, mixed oxide powder, composite powder reduced at 350°C, 700°C, and 800°C.

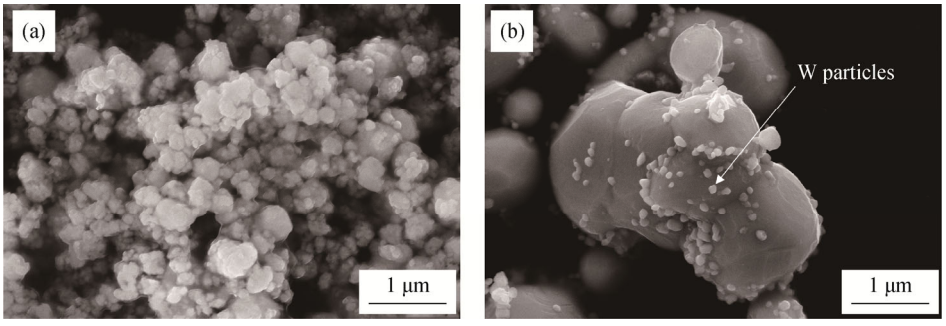

Fig. 5. SEM images of mixed oxide powder (a) and composite powder reduced at 800°C (b).

Fig. 6 shows the microstructure of the Cu–3W, Cu–6W, and Cu–10W composites obtained using SEM under the BSE mode and Fig. 7 shows the average particle size of W in the Cu–W composites with different W content. Compared to the Cu–3W composite (Fig. 6(a)), W particles in the composite with higher tungsten content (Fig. 6(b) and Fig. 6(c)) were more easily agglomerated. As noted in Fig. 6(c), the W clusters were several small particles grouped, which is consistent with that of a reduced powder shown in Fig. 5(b). As shown in the Fig. 7, with increasing tungsten content, the average particle size changed from 119 nm for Cu–3W to 151 nm for Cu–6W and 199 nm for Cu–10W. Fig. 6 and Fig. 7 indicate that for composites with higher W content, tungsten particles tend to be agglomerated and form larger particles. To measure the particle distribution of W particles with different sizes, a high magnification BSE-SEM image of a deeply etched Cu–10W sintered specimen is shown in Fig. 8. Areas 1 and 2 in Fig. 8 were related to the grain boundaries and the inner grains, respectively. W nanoparticles inside the Cu grains were only about 20–50 nm in diameter. The white W particles on the grain boundaries were obviously larger than those on the grains. This phenomenon can be attributed to the difference in the nucleation location of the W particles. The W particles nucleated on the Cu powder surface tend to grow without limit during the reducing procedure. In the sintering process, the large W particles will impede the growth of Cu grains in the bulk composite [30]. Alternatively, the growth of the W particles inside the Cu grains is constrained, so the W particles were also smaller.

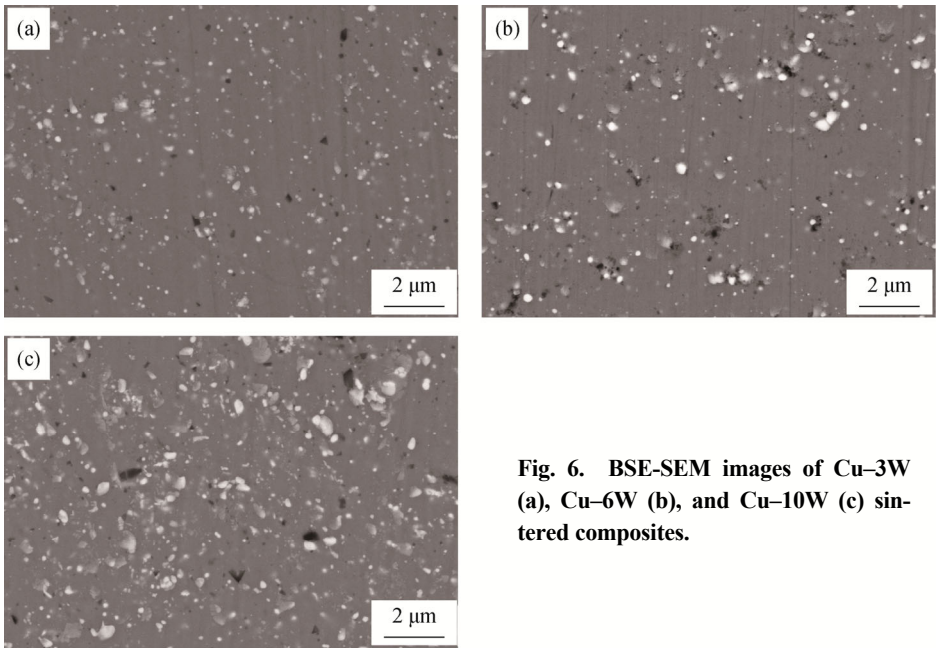

Fig. 6. BSE-SEM images of Cu–3W (a), Cu–6W (b), and Cu–10W (c) sintered composites.

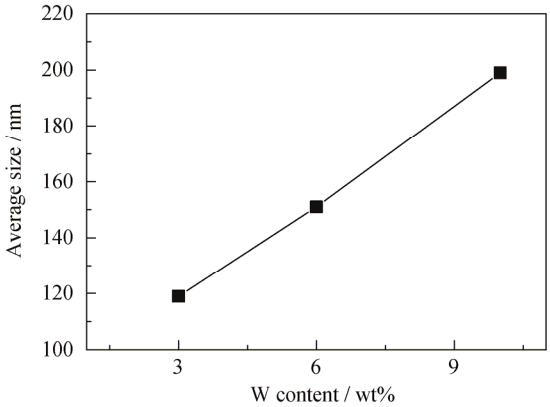

Fig. 7. Average W particle size statistic of composites with different W content.

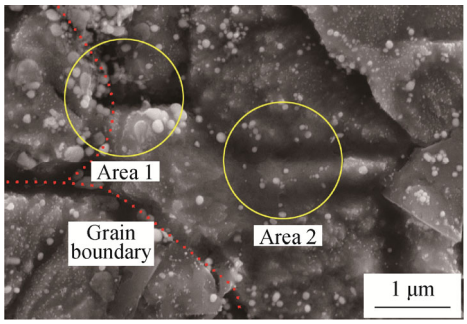

Fig. 8. High-magnitude BSE-SEM image of the Cu–10W sintered specimen.

Fig. 9(a) is a typical bright-field TEM image of Cu–6W bulk composite. The W particles (indicated by arrows) had a

similar size and characterization, which are presented in the SEM images (Fig. 6(b)). To illustrate the detailed microstructures of the Cu matrix and W particles, the HAADF-STEM images were displayed in Fig. 9(b). In the Cu matrix, W particles were mainly located at the copper grain boundaries. As shown in Fig. 9(c), the EDS results proved that there was no tungsten solid solution in the copper matrix. An HR-TEM micrograph of the Cu matrix and W particle interface is provided in Fig. 9(d). In this micrograph, the interplanar distance of the matrix and second phase particle were 0.209 nm and 0.225 nm, corresponding to the lattice plane (111) of Cu and (110) of W, respectively. The interfaces between the Cu and W particles were tightly bonded, promoting electron transport to minimize the loss of electrical conductivity because electrons will transport through the interface between the Cu and W with less resistance.

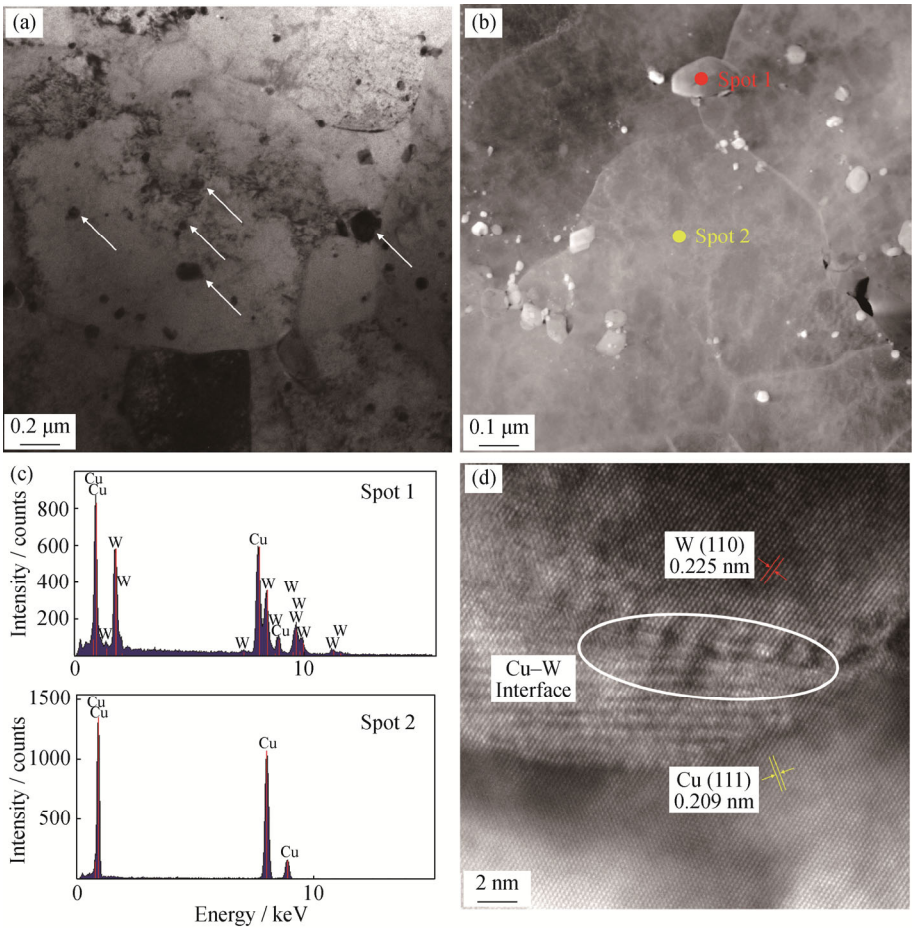

Fig. 9. TEM analysis results of Cu–6W bulk composite: (a) bright-field TEM images; (b) HAADF-STEM image; (c) EDS results for spots 1 and 2 in (b); (d) HR-TEM micrograph of the Cu-W interface.

3.3. Mechanical properties and electrical conductivity

Fig. 10 and Fig. 11 show the ultimate tensile strength, yield strength, elongation, Vickers hardness of the sintered pure Cu and Cu–W samples. The addition of W nanoparticles significantly improves the hardness and strength of the composite. According to the tensile test results, the tensile strength of bulk Cu–W composites were continuously enhanced with increasing content of tungsten up to 6wt%. The Cu–6W had the best mechanical properties with a tensile strength of 310 MPa, yield strength of 238 MPa, and Vickers hardness of HV 108, which were 26%, 230%, and 74% greater than pure copper, respectively. However, the tungsten content greater than 6wt% does not improve the strength of the Cu–W composites. Compared to the Cu–6W sample, the tensile strength and elongation of Cu–10W decreased simultaneously. The main reason for this phenomenon is the influence of large W particles. In the Cu–10W composite, several large particles and W clusters (larger than 500 nm) remarkably reduced the ductility of the copper matrix and formed the source of the cracks during the loading. Furthermore, the agglomeration of large particles will also hinder densification of the copper matrix. Fig. 12 shows the SEM images of the Cu–6W and Cu–10W fracture. As shown in the SEM images, the W particles in Cu–10W tend to aggregate more than in Cu–6W. As a result, the mechanical properties of Cu–10W were restricted by large W particles.

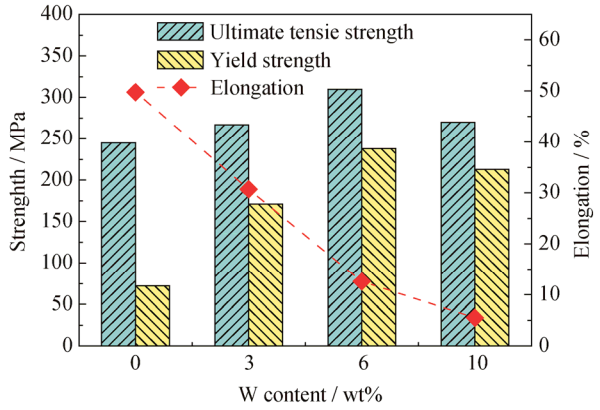

Fig. 10. Ultimate tensile strength, yield strength, and elongation of pure copper and Cu–W composites with different W contents.

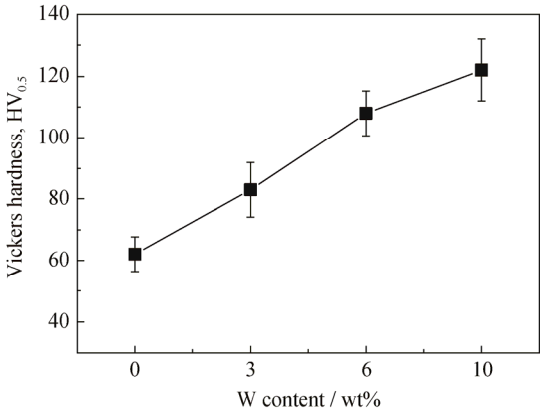

Fig. 11. Vickers hardness of pure copper and Cu–W composites with different W content.

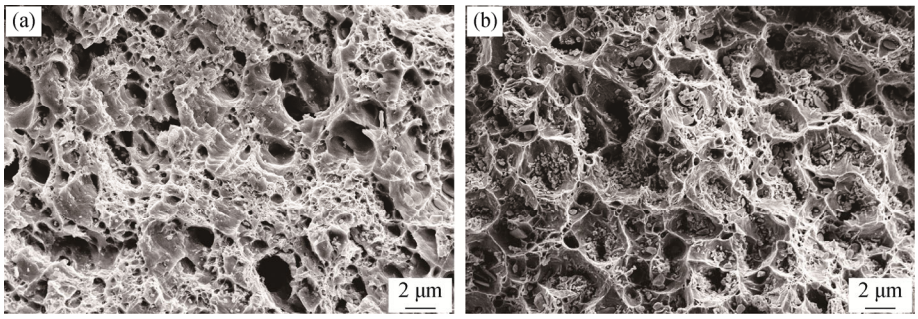

Fig. 12. Fracture SEM images of Cu–6W (a) and Cu–10W(b).

The electrical conductivity of the composites is shown in Fig. 13. Based on the conductivity results, Cu–3W (Cu–1.5vol%W) and Cu–6W (Cu–3vol%W) provided only less than a 10% decrease in the electrical conductivity. Even for the Cu–10W composite, the electrical conductivity was maintained at 84% IACS. Compared with a commercial alumina dispersion strengthened (ODS) copper alloy [31], the electrical conductivity of the W nanoparticles was much greater at the same content fraction. Reinforced Cu composites with W nanoparticles show superior application potential due to adequate mechanical and electrical properties.

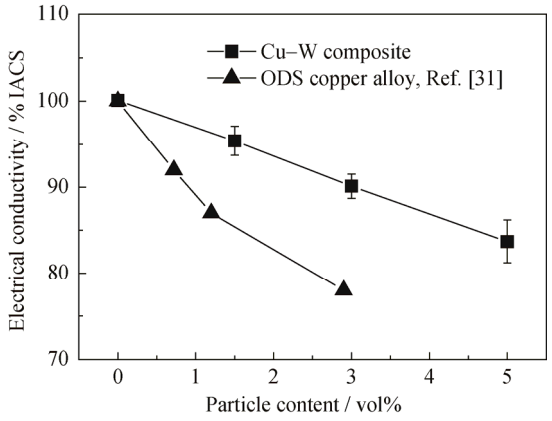

Fig. 13. Electrical conductivity of Cu–W composites and ODS copper alloy.

4. Conclusions

W nanoparticle-strengthened Cu composites were prepared from nanopowders synthesized by a sol–gel method Ultrafine W particles were uniformly dispersed in the copper matrix, significantly enhanced the strength and hardness of the copper composite. The Cu–W composite with 6wt% tungsten had the best comprehensive properties with a tensile strength of 310 MPa, hardness of HV 108, and only 10% loss of the electrical conductivity compared to pure Cu. With an increase in the tungsten content in the copper matrix, the average particle size of W particle increased from 119 nm for Cu–3W to 199 nm for Cu–10W, whereas the elongation and electrical conductivity decreased. The agglomeration of large particles would affect the elongation of composites when the tungsten content increases.

Acknowledgements

This work was supported by the Fundamental Research Funds for the Central Universities (No. FRF-TP-18-029A2) and State Key Lab of Advanced Metals and Materials of China (No. 2019-Z10).

References

[1] G. Li, B.G. Thomas, and J.F. Stubbins, Modeling creep and fatigue of copper alloys, *Metall. Mater. Trans. A*, 31(2000), No. 10, p. 2491.

[2] G. Carro, A. Muñoz, M.A. Monge, B. Savoini, R. Pareja, C. Ballesteros, and P. Adeva, Fabrication and characterization of Y_2O_3 dispersion strengthened copper alloys, *J. Nucl. Mater.*, 455(2014), No. 1-3, p. 655.

[3] S.J. He, Y.B. Jiang, J.X. Xie, Y.H. Li, and L.J. Yue, Effects of Ni content on the cast and solid-solution microstructures of Cu–0.4wt%Be alloys, *Int. J. Miner. Metall. Mater.*, 25(2018), No. 6, p. 641.

[4] J. Groza, Heat-resistant dispersion-strengthened copper alloys, *J. Mater. Eng. Perform.*, 1(1992), No. 1, p. 113.

[5] E. Karakulak, Characterization of Cu–Ti powder metallurgical materials, *Int. J. Miner. Metall. Mater.*, 24(2017), No. 1, p. 83.

[6] D.W. Lee and B.K. Kim, Nanostructured Cu–Al_2O_3 composite produced by thermochemical process for electrode application, *Mater. Lett.*, 58(2004), No. 3-4, p. 378.

[7] A. Wagih and A. Fathy, Improving compressibility and thermal properties of Al–Al_2O_3 nanocomposites using Mg particles, *J. Mater. Sci.*, 53(2018), No. 16, p. 11393.

[8] C. Suryanarayana and N. Al-aqeeli, Mechanically alloyed nanocomposites, *Prog. Mater. Sci.*, 58(2013), No. 4, p. 383.

[9] S.J. Hwang and J.H. Lee, Mechanochemical synthesis of Cu–Al_2O_3 nanocomposites, *Mater. Sci. Eng. A*, 405(2005), No. 1-2, p. 140.

[10] S.M.S. Aghamiri, N. Oono, S. Ukai, R. Kasada, H. Noto, Y. Hishinuma, and T. Muroga, Brass-texture induced grain structure evolution in room temperature rolled ODS copper, *Mater. Sci. Eng. A*, 749(2019), p. 118.

[11] A. Abu-Oqail, A. Wagih, A. Fathy, O. Elkady, and A.M. Kabeel, Effect of high energy ball milling on strengthening of Cu–ZrO_2 nanocomposites, *Ceram. Int.*, 45(2019), No. 5, p. 5866.

[12] A. Wagih, A. Abu-Oqail, and A. Fathy, Effect of GNPs content on thermal and mechanical properties of a novel hybrid Cu–Al_2O_3/GNPs coated Ag nanocomposite, *Ceram. Int.*, 45(2019), No. 1, p. 1115.

[13] M. Baghani, M. Aliofkhazraei, and M. Askari, Cu–Zn–Al_2O_3 nanocomposites: study of microstructure, corrosion, and wear properties, *Int. J. Miner. Metall. Mater.*, 24(2017), No. 4, p. 462.

[14] M. Baghani and M. Aliofkhazraei, CuCrW(Al_2O_3) nanocomposite: mechanical alloying, microstructure, and tribological properties, *Int. J. Miner. Metall. Mater.*, 24(2017), No. 11, p. 1321.

[15] F. Chi, M. Schmerling, Z. Eliezer, H.L. Marcus, and M.E. Fine, Preparation of Cu–TiN alloy by external nitridation in combination with mechanical alloying, *Mater. Sci. Eng. A*, 190(1995), No. 1-2, p. 181.

[16] S.C. Tjong and K.C. Lau, Tribological behaviour of SiC particle-reinforced copper matrix composites, *Mater. Lett.*, 43(2000), No. 5-6, p. 274.

[17] J.R. Groza and J.C. Gibeling, Principles of particle selection for dispersion-strengthened copper, *Mater. Sci. Eng. A*, 171(1993), No. 1-2, p. 115.

[18] L.L. Dong, M. Ahangarkani, W.G. Chen, and Y.S. Zhang, Recent progress in development of tungsten-copper composites: Fabrication, modification and applications, *Int. J. Refract. Met. Hard Mater.*, 75(2018), p. 30.

[19] Z.M. Xie, R. Liu, S. Miao, X.D. Yang, T. Zhang, X.P. Wang, Q.F. Fang, C.S. Liu, G.N. Luo, Y.Y. Lian, and X. Liu, Extraordinary high ductility/strength of the interface designed bulk W–ZrC alloy plate at relatively low temperature, *Sci. Rep.*, 5(2015), art. No. 16014.

[20] M.A. Atwater, D. Roy, K.A. Darling, B.G. Butler, R.O. Scattergood, and C.C. Koch, The thermal stability of nanocrystalline copper cryogenically milled with tungsten, *Mater. Sci. Eng. A*, 558(2012), p. 226.

[21] T. Raghu, R. Sundaresan, P. Ramakrishnan, and T.R. Rama Mohan, Synthesis of nanocrystalline copper-tungsten alloys by mechanical alloying, *Mater. Sci. Eng. A*, 304-306(2001), p. 438.

[22] Y.J. Guo, H.T. Guo, B.X. Gao, X.G. Wang, Y.B. Hu, and Z.Q. Shi, Rapid consolidation of ultrafine grained W–30wt%Cu composites by field assisted sintering from the sol–gel prepared nanopowders, *J. Alloys Compd.*, 724(2017), p. 115.

[23] Y.W. Jiang, S.G. Yang, Z.H. Hua, and H.B. Huang, Sol–gel autocombustion synthesis of metals and metal alloys, *Angew. Chem. Int. Ed.*, 48(2009), No. 45, p. 8529.

[24] S. Mula, D. Setman, K. Youssef, R.O. Scattergood, and C.C. Koch, Structural evolution of $Cu_{(1-X)}Y_X$ alloys prepared by mechanical alloying: Their thermal stability and mechanical properties, *J. Alloys Compd.*, 627(2015), p. 108.

[25] A.R. Miedema, P.F. de Chatel, and F.R. de Boer, Cohesion in alloys—Fundamentals of a semi-empirical model, *Physica B+C*, 100(1980), No. 1, p. 1.

[26] M. Ardestani, H. Arabi, H. Razavizadeh, H.R. Rezaie, B. Jankovic, and S. Mentus, An investigation about the activation energies of the reduction transitions of fine dispersed $CuWO_{4-x}/WO_{3-x}$ oxide powders, *Int. J. Refract. Met. Hard Mater.*, 28(2010), No. 3, p. 383.

[27] Y. Zhou, Q.X. Sun, R. Liu, X.P. Wang, C.S. Liu, and Q.F. Fang, Microstructure and properties of fine grained W–15wt%Cu composite sintered by microwave from the sol–gel prepared powders, *J. Alloys Compd.*, 547(2013), p. 18.

[28] A.K. Basu and F.R. Sale, Copper-tungsten composite powders by the hydrogen reduction of copper tungstate, *J. Mater. Sci.*, 13(1978), No. 12, p. 2703.

[29] K.F. Wang, G.D. Sun, Y.D. Wu, and G.H. Zhang, Fabrication of ultrafine and high-purity tungsten carbide powders via a carbothermic reduction–carburization process, *J. Alloys Compd.*, 784(2019), p. 362.

[30] S.N. Alam, Synthesis and characterization of W–Cu nanocomposites developed by mechanical alloying, *Mater. Sci. Eng. A*, 433(2006), No. 1-2, p. 161.

[31] North American Hoganas High Alloys LLC, *GLIDCOP® Dispersion Strengthened Copper,* North American Hoganas High Alloys LLC, Pennsylvania [2019-7-25]. https://www.hoganas.com/en/powder-technologies/glidcop